Fast Interleaved Echo-Planar Imaging with Navigator: High Resolution Anatomic and Functional Images at 4 Tesla

Seong-Gi Kim, Xiaoping Hu, Gregor Adriany, Kâmil Uğurbil

Echo-planar imaging (EPI) is sensitive to magnetic field inhomogeneities, which lead to signal loss and geometric distortions of the image. Magnetic field inhomogeneities induced by susceptibility differences, as encountered in the human body, increase with the magnetic field strength, thus, complicating implementation of high resolution EPI techniques on high magnetic field systems. These problems were overcome by using a fast multishot high resolution EPI method that uses variable flip angles, center-out *k*-space sampling, and navigator echoes. This approach maximizes signal-to-noise ratio, reduces flow artifacts, and permits correction of intersegment amplitude and phase variations, providing high spatial and temporal resolution. This scheme can be implemented with a single magnetization preparation for contrast that precedes the segments. The utility of this ultrafast segmented EPI technique with navigator is demonstrated for anatomic and functional imaging studies on the human brain at 4 T.

Key words: Echo-planar imaging; navigator; high resolution imaging; functional MRI.

INTRODUCTION

Echo-planar imaging (EPI), first proposed by Mansfield, permits the acquisition of the *k*-space data for a single image in less than 100 ms (1). This method requires special hardware such as gradient sets with fast switching rates and fast digitizers. Unfortunately, EPI images are sensitive to susceptibility/chemical shift artifacts, which lead to geometric distortions (2, 3). These problems are especially severe at high magnetic fields because the susceptibility and chemical shift effects are proportional to magnetic field strength. Consequently, EPI has not been widely used for anatomic neuroimaging. Recently, the advent of functional brain mapping (4–12) has intensified the interest in EPI techniques because of the high temporal resolution and high signal-to-noise ratio (SNR) that can be obtained for multislice acquisitions.

Signal detection in EPI is limited by T_2* relaxation because the data acquisition is performed during repetitive gradient echoes. The T_2* of tissue at high magnetic fields is shorter than that at low magnetic fields. Therefore, it is difficult to acquire a high resolution EPI image in a *single-shot* on high field systems. An alternative approach is to employ a *multishot*, interleaved, *k*-space data collection scheme (13–16). However, because repeated RF pulses create magnetization saturation, a long delay time between segments is needed or dummy scans are required until a steady-state condition is reached, leading to prolonged acquisition times. Thus, this method is sensitive to physiological or rigid body motions. Another strategy is to use low flip angle RF pulses as in conventional fast low angle shot (FLASH) techniques, albeit resulting in low SNR. Imaging time can be reduced and SNR maximized using a variable RF flip angle approach with a minimum intersegment delay time (13, 17, 18).

In segmented schemes, the magnitude and phase of each segment can vary because of imperfect RF flip angle, physiological motion, and the approach to the steady state. These variations will create higher ghosting and blurring effects in images, causing more interimage variations. To monitor and correct these variations, navigator echoes can be acquired before the application of phase-encoding gradients similar to those used in conventional imaging techniques (19, 20). The navigator echo is the profile of readout direction and can be used to correct intersegment variations.

When *k*-space data of blipped EPI images are sampled sequentially from the bottom to the top (bottom-top) of *k*-space lines, low *k*-space points that determine signal intensities are acquired at the middle of the gradient echo train. Therefore, EPI images suffer signal loss caused by T_2* weighting. This problem exists especially in anatomic images with magnetization preparation, which need a short echo time to preserve prepared magnetization. To maximize SNR with a short effective echo time, we have implemented a sampling scheme that covers *k*-space along the phase-encoding direction in the center-out fashion (13). In the T_1-weighted images, this scheme will enhance SNR and T_1 contrast.

Flow effects in EPI images are complicated (21–24). Because EPI requires oscillating gradients for the readout direction (kx), phases at $kx = 0$ will be shifted at odd echoes and refocused at even echoes because of constant velocity flow, causing ghosts, blurring, and shifting. Flow in the phase-encoding direction also causes flow artifacts because each *k*-space line (ky) has a different degree of dephasing. When the conventional bottom-top phase-encoding steps are used, the zero *k*-space line ($ky = 0$) contains a non-zero first moment because of flow, adding up artifacts. The center-out sampling scheme will be helpful to reduce flow artifacts because of a zero first moment at $ky = 0$.

MRM 35:895–902 (1996)

From the Center for Magnetic Resonance Research, Department of Radiology, University of Minnesota Medical School, Minneapolis, Minnesota.

Address correspondence to: Seong-Gi Kim, Ph.D., CMRR, University of Minnesota Medical School, 385 E. River Road, Minneapolis, MN 55455.

Received October 6, 1995; revised January 19, 1996; accepted January 22, 1996.

This work was supported by National Institutes of Health Grants RR08079, NS32919, and NS32437 and by a Grant-in-Aid from the University of Minnesota.

0740-3194/96 $3.00

In this paper, we describe an approach that brings together several concepts, each of which have been used separately, to remedy various problems in high speed imaging. The technique includes variable flip angle, center-out sampling, and minimum intersegment delay to increase SNR and temporal resolution, and navigator echoes to correct for intersegment phase and amplitude variations. The effectiveness of this approach in obtaining high speed images with a single magnetization preparation for contrast generation has been demonstrated. The new scheme permitted the acquisition of high resolution anatomic and functional images even at 4 T.

TECHNIQUE

EPI was implemented with trapezoidal gradient shapes for the readout and blipped gradients for the phase-encoding direction. If the frequency-encoded data are collected only during the plateau of the readout gradient, the data acquisition can become quite long. For example, a single-shot image with a matrix size of 128 × 128 over a field of view (FOV) of 20 × 20 cm^2 acquired at a digitization rate of 200 kHz requires 82 ms for sampling data and, in our system, 40 ms for switching gradients. To collect the image faster, we acquired 160 complex pairs during both gradient rise/fall (with nonlinear *k*-space sampling) and plateau (with linear *k*-space sampling) periods. These nonlinear *k*-space data were sinc-interpolated to 128 linear points (25). The acquisition time of each *k*-space line (*kx*) was 0.8 ms and the total acquisition time for a 128 × 128 matrix was 102.4 ms. Because T_2* of the brain tissues is approximately 40 ms at 4 T, it is almost impossible to acquire high resolution images as a single shot. Thus, an interleaved segmentation was implemented. Generally four segments were applied and 32 phase-encoding steps were acquired in each segment during a period of 25.6 ms.

A segmented EPI technique was implemented to obtain high spatial and temporal resolution and maximum SNR. Figure 1 shows a segmented EPI pulse sequence and *k*-space sampling trajectory. Each acquisition following an RF pulse is repeated by the number of segments (N_{seg}) with different RF flip angles and blipped gradient signs. Odd segments employ positive blipped gradients, whereas even segments employ negative blipped gradients. After the RF pulse and a delay time for T_2* weighting were applied (when required), a *k*-space line (i.e., navigator echo) was acquired at the beginning of each segment in the absence of the phase-encoding gradient (shown in the box filled with dots). Subsequently, *k*-space lines were acquired with the interleaved center-out sampling scheme, in which the first segment is acquired from the center to the top of the *k*-space and next segment is from the center to the bottom of the *k*-space shown as Fig. 1b. The strength of the first blipped gradient is less than that of the others. A crushing gradient was applied at the end of the data collection for each segment to suppress stimulated echoes caused by repeated RF pulses.

To improve SNR, variable flip angles were used. Generally, optimal flip angles for each segment are dependent on repetition time (*TR*), T_1, and the flip angle of a preceding pulse (13). Variable flip angles can only be optimized to a single T_1 component if the longitudinal relaxation is significant. However, if the *TR* of each segment is relatively short compared with T_1 of tissues, this contribution is minimal. At 4 T, T_1 of gray and white matter is 1.35 and 0.9 s, respectively (26). Because the

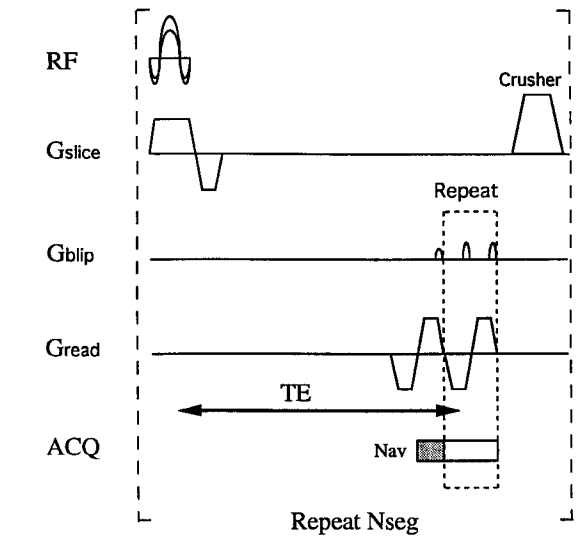

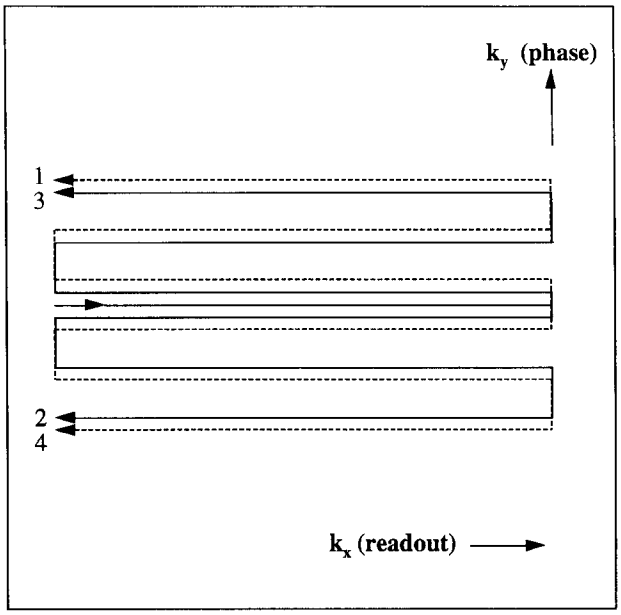

FIG. 1. Echo planar imaging pulse sequence (a) and *k*-space sampling trajectory (b) with segmentation, center-out sampling, variable RF flip angles, and navigator echoes. Each segment is repeated at the number of segments (N_{seg}). G_{slice} represents the slice-selection gradient; G_{blip}, blipped phase-encoding gradient; G_{read}, readout gradient; ACQ, data acquisition; *TE*, echo time; Nav, navigator echo data collection (the box filled with dots); *kx*, *k*-space in the *x* (readout) direction; and *ky*, *k*-space in the *y* (phase-encoding) direction. Numbers in (b) indicate the interleaved sampling orders. Crushing gradient (Crusher) was applied with a slice-selection gradient at the end of each segment.

repetition time of each segment was 40–60 ms, it is permissible to ignore the T_1 contribution. The flip angle of the n − 1th segment, α_{n-1}, can be calculated from the flip angle of the nth segment, α_n, using $\alpha_{n-1} = \tan^{-1}[\sin(\alpha_n)]$. For maximum signal, the excitation pulse for the last segment was set to 90°. For all four segments, the flip angles used were 30, 35, 45, and 90°, respectively (13).

Because the gradient echoes were collected with a readout gradient of alternating polarity, even and odd echoes had opposite *k*-space orders and, thus, alternated *k*-space lines were time-reversed. During the data collection, echo positions of the even and odd echoes may not line up because of gradient imperfection, eddy currents, and off-resonance effects, causing artifacts. To correct those artifacts, we acquired a reference image without the application of phase-encoding gradients. The phases from reference data were used to correct phases of the imaging data (25). For each slice, a reference image was separately acquired and phase correction was performed slice by slice. This correction was found useful in improving image quality.

To detect and correct signal modulations between segments, each navigator signal was Fourier transformed to produce projection along the readout direction. All correction was performed on a point-by-point basis in the projection space. The magnitude of each navigator point in each segment was determined first, then the magnitudes were averaged for all segments ("average magnitude"). The ratio between the average magnitude and the magnitude of each navigator was used to correct the corresponding points of each segment. For phase correction, the phase of each point in navigator projection was determined. Then, the amount of phase needed to set phase of the navigator projection to zero was used to correct the corresponding points of the same segment. This phase correction is nonlinear along the projection direction. These magnitude and phase corrections were performed for the segments within each image, but were not used for correcting interimage variations when sequential images were acquired as in functional brain mapping studies.

METHODS AND MATERIALS

Magnetic resonance imaging studies were performed with a 4 T whole body imaging system with a 1.25-m diameter bore (SISCO, Palo Alto, CA/Siemens, Erlangen, Germany) and a head gradient insert with a gradient strength of 30 mT/m and a slew rate of 150 T/m/s in all three axes. For RF transmission and detection, a homogeneous birdcage was used. Manual shimming was performed to improve homogeneity before the EPI data collection.

All four-segmented EPI images were acquired by the scheme shown in Fig. 1. The magnitude correction was performed between segments using navigator echoes. Typical parameters were a matrix size of 128 × 128, FOV of 20 × 20 cm^2, and a slice thickness of 5 mm. High resolution T_1-weighted EPI images were obtained by sequential acquisition of each segment without any additional intersegment delay after a *single* inversion pulse and a subsequent delay. Adiabatic pulses were used for inversion preparation. Parameters were a *TE* of 8 ms, *TR* for each segment of 40 ms, and *TI* of 1.2 s. In high resolution T_2*-weighted EPI images for functional imaging studies, the effective *TE* was 25 ms and the imaging time for a single image was 240 ms.

To compare bottom-top and center-out sampling schemes, images were acquired with the identical imaging parameters. Data were acquired at 8–33.6 ms after an RF pulse and effective echo times were 8 and 20.8 ms for center-out and bottom-top sampling schemes, respectively. The *TR* of each segment was 40 ms.

For functional imaging studies, T_2*-weighted EPI images were acquired repeatedly during consecutive resting (no stimulation) and stimulation periods. Ten coronal 5-mm thick slices were chosen to cover the calcarine fissure in the visual cortex. For visual stimulation, light-tight goggles containing LED arrays (Grass Instruments, Quincy, MA) with an 8 Hz flash frequency were used. Functional activation maps were calculated using a cross-correlation method with a boxcar reference wave form on a pixel-by-pixel basis (27). Functional activation maps were overlaid on T_1-weighted EPI images to identify activation sites.

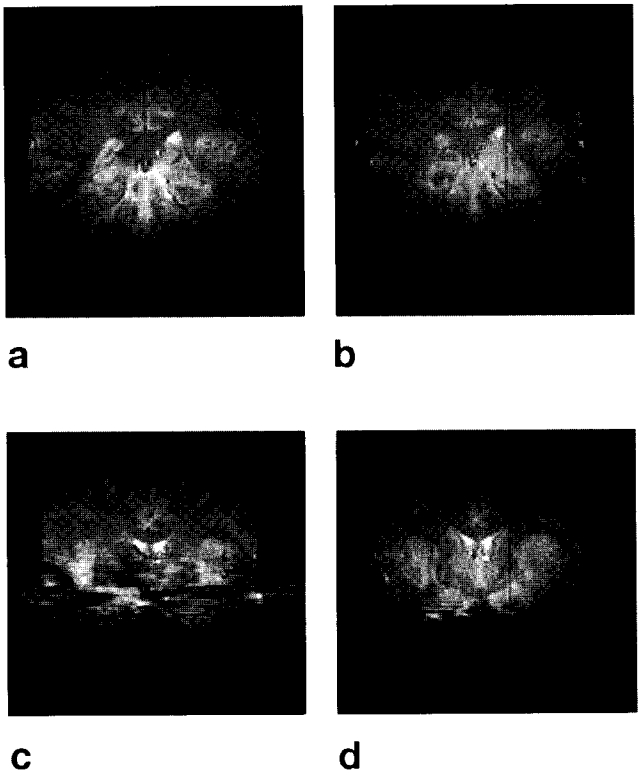

FIG. 2. High-resolution T_2*-weighted coronal EPI images acquired using the bottom-top (a) and (c) and the center-out (b) and (d) sampling schemes with variable RF flip angles and an intersegment time of 40 ms. With four segments, an imaging time was 160 ms. In-plane resolution was 1.56 × 1.56 mm^2 with 5-mm slice thickness. Because signal intensities of (b) and (d) were approximately 25% higher than those of (a) and (c), image display was adjusted by 25%, so that images can be compared. All imaging parameters were identical. Phase-encoding direction is horizontal.

RESULTS

To compare the effects of phase-encoding schemes, coronal four-segmented images (128 × 128) acquired with the identical imaging parameters are shown in Fig. 2. These images were collected with the conventional bottom-top (Figs. 2a and 2c) and the center-out (Figs. 2b and 2d) phase-encoding schemes. Many different effects can be observed. First, since a zero *k*-space line was acquired at different time points (effective *TE* of 8 and 20.6 ms for center-out and bottom-top, respectively), image contrast is different. Average signals of images acquired using the bottom-top scheme were approximately 25% less than those of center-out images because of T_2* decay of tissue signal. Thus, image display was adjusted by 25% to compare images. Because T_2* of cerebrospinal fluid (CSF) is longer than T_2* of gray and white matter, relative intensity of ventricle areas containing CSF at the middle of brain is brighter in the bottom-top than in the center-out images. Second, artifacts in the phase-encoding direction were evident in the images acquired with the bottom-to-top scheme, especially in Fig. 2c, and these artifacts were significantly reduced in the images collected with the center-out scheme. However, there were still residual artifacts in Fig. 2d, which could be reduced further by more segments. Third, careful inspection of these images shows different chemical shift and filtering effects. These effects will be discussed later.

Because multiple shots were used to acquire a single image, it is important to monitor and correct fluctuations of signals between segments regardless of phase-encoding schemes. Figure 3 shows magnitude and phase fluctuations of the navigator echoes in T_2*- and T_1-weighted images of a single coronal slice. Especially in a T_1-weighted image (Fig. 3b), magnitude variations are greater than those in a T_2*-weighted image (Fig. 3a) because of additional T_1 relaxation. Average variations of each segment were −14 ~ 28% and −26 ~ 45% of the average magnitudes in the T_2*- and T_1-weighted images, respectively. Phases of readout points between 20 and 90 with sufficient SNR were determined from T_2*- (Fig. 3c) and T_1-weighted (Fig. 3d) images. In most of points, phase variations between segments were within 0.1 radian. Large phase variations were seen at a readout point 20 because of low SNR. Figure 4 shows images with

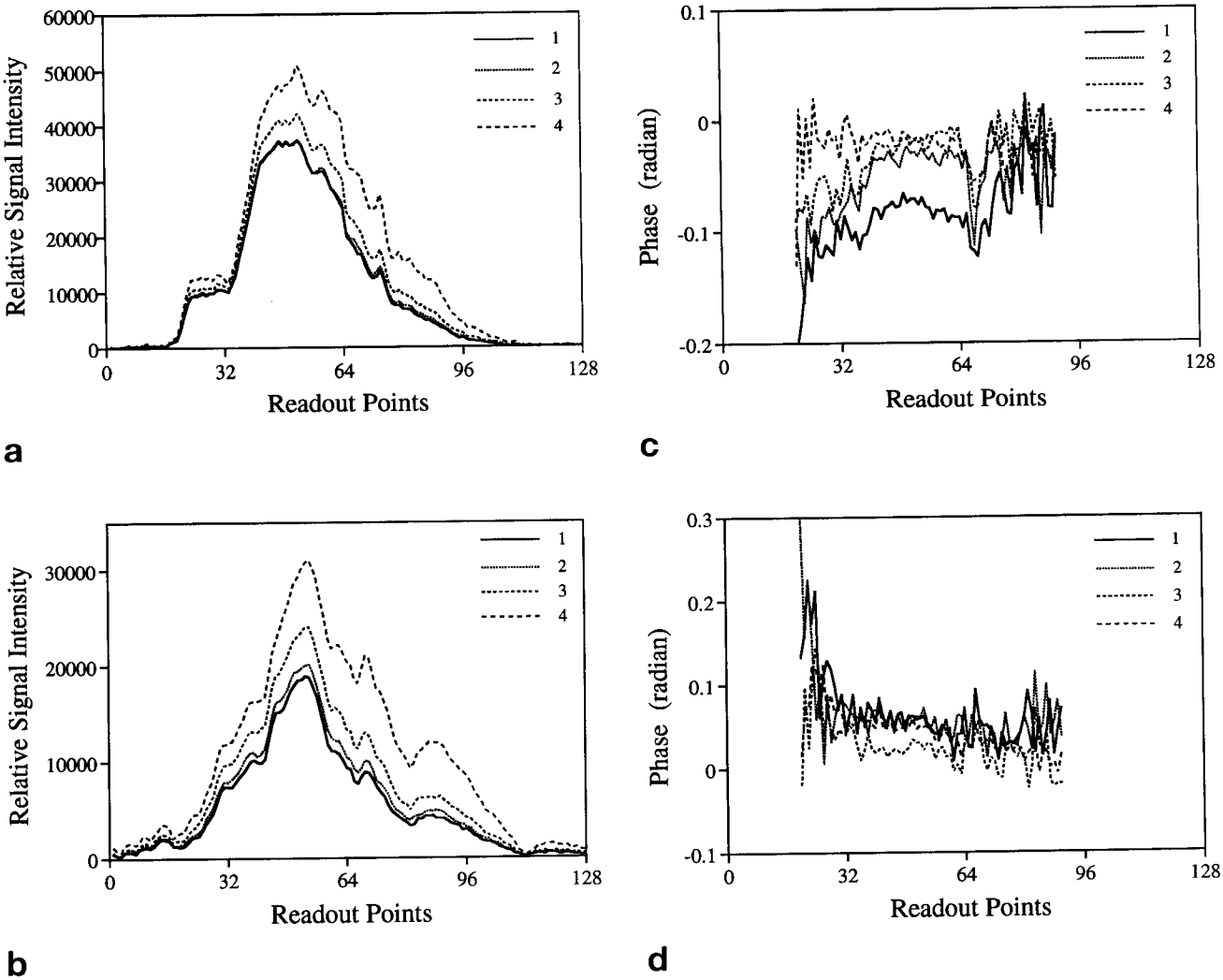

FIG. 3. Magnitude (a) and (b) and phase (c) and (d) of navigator readout *k*-space lines in T_2*-weighted (a) and (c) and T_1-weighted (b) and (d) images. The number in plots indicates the order of segments acquired. Phase was calculated at the readout points between 20 and 90.

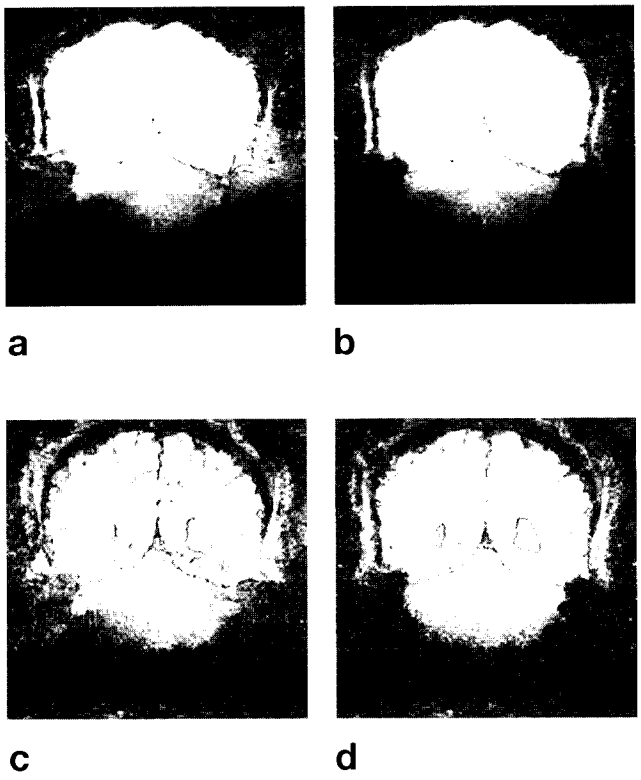

FIG. 4. High resolution T_2*-weighted (a) and (b) and T_1-weighted (c) and (d) images without (a) and (c) and with (b) and (d) magnitude correction using navigator signals shown in Fig. 3. To visualize the effectiveness of the magnitude correction, image display was adjusted.

(Figs. 4b and 4d) and without (Figs. 4a and 4c) magnitude corrections of the data shown in Fig. 3. To demonstrate the effectiveness of magnitude corrections, image display was adjusted so that segmentation artifacts can be visualized easily in background. Clearly, there are less segmentation artifacts in both T_2*- (Fig. 4b) and T_1-weighted (Fig. 4d) images with the magnitude correction.

Figure 5 shows high resolution T_1-weighted coronal images acquired in four segments after a single inversion pulse. Image quality and contrast are excellent and white and gray matter areas can be identified easily. These images can be used to identify the location of "activation" detected in T_2*-weighted EPI images. In functional imaging studies, it is important to compare against anatomic images with the same imaging scheme. Otherwise, image registration between functional and anatomic images will be problematic, especially at regions with high local susceptibility.

High resolution functional imaging was examined during visual stimulation. Figure 6 shows multislice coronal T_2*-weighted EPI (Fig. 6A) and functional maps overlaid on the anatomic EPI images (Fig. 6B). The effective *TE* of T_2*-weighted images was 25 ms and the imaging time of a single slice was 240 ms. Voxel resolution is $1.56 \times 1.56 \times 5.0$ mm^3 in both anatomic and functional images. Ten 5-mm slices were collected at every 5 s and only nine posterior slices were presented here. In T_2*-weighted images, gray and white matter contrast is good and large venous vessels with low signal intensities can be identified because of the short T_2* of deoxygenated blood. Importantly, phase-encoding artifacts were minimal since the high resolution scheme with navigator echo correction was used. During visual stimulation, signal changes were located predominantly at the visual area, especially in the gray matter areas. This is consistent with previous studies (4, 8). Large signal changes were also observed in the superior sagittal sinus at the most posterior slice caused by macrovascular inflow effects and in the straight sinus caused by macrovascular blood oxygen level dependent effects. Such macrovascular effects can be eliminated using other strategies such as bipolar gradients. Note that there is no significant negative signal change during visual stimulation.

DISCUSSION

In our segmentation scheme, variable flip angles and a minimal intersegment delay were used to increase SNR and temporal resolution, resulting in decrease of motion problems. Multi-segmented data can be acquired rapidly after magnetization preparation. Thus, this technique is well-suited for the magnetization-prepared images such as T_1-weighted EPI. In the single slice functional imaging studies, the same slice will be acquired repeatedly. In this case, the magnetization with a constant flip angle will reach the steady-state condition quickly after dummy scans (such as FLASH) and therefore it is not an advantage to use variable flip angles. However, in the multislice functional activation studies with high spatial resolution, multislice images take several seconds (Fig. 6). In this case, the variable flip angle approach is beneficial.

The navigator *k*-space line was acquired at every segment and its amplitude and phase can be used to correct the subsequently collected *k*-space lines. Magnitude correction is crucial to reduce segmentation artifacts (Fig. 3). In some cases with high B_1 inhomogeneity, variable flip angles can lead to signal differences among the segments. Generally, flip angles are not calibrated and coils are not tuned at every imaging session. Depending on the load (i.e., head size), tuning of the coil can vary and subsequently calibration of flip angles will be different, creating signal differences between segments. This problem will be more serious when inhomogeneous surface coils are used. Furthermore, we assumed that relaxation between segments would be minimal and thus did not include the T_1 term in calculating flip angles. This may not be correct especially in T_1-prepared EPI. Thus, magnitude will vary at different readout positions depending on B_1 and T_1. These problems can be identified and eased by magnitude corrections using navigator signals. In contrast, the major sources of phase variations are respiration (ca. 0.3 Hz) and cardiac pulsation (ca. 1.0 Hz) (19, 28, 29). Because each high resolution T_2*-weighted image was acquired within 240 ms, phase modulation within an image was minimal. Thus, phase correction did not significantly improve the functional MRI data. When many segments and a long data acquisition time are employed such as in three-dimensional (3D) EPI, phase variations become significant because of physiological motions, resulting in high intersegment fluctuations. In this case, phase correction would be useful (19).

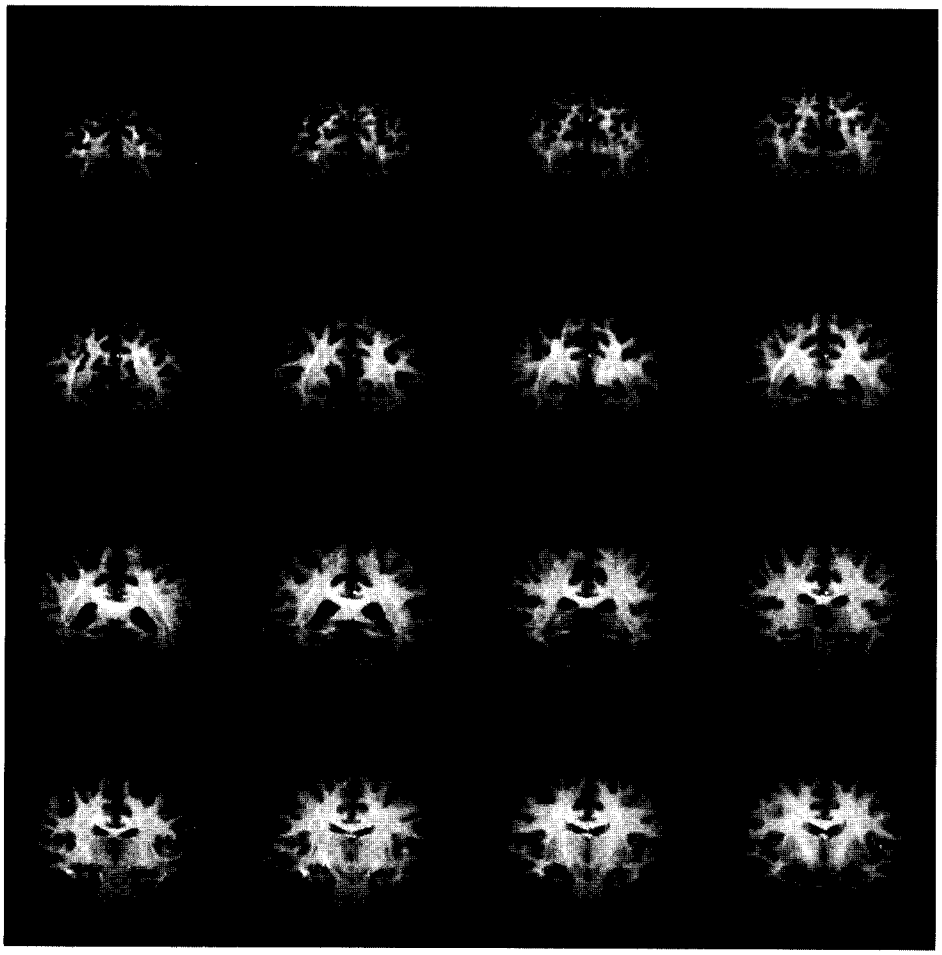

FIG. 5. Multislice four-segmented coronal T_1-weighted EPI images. A single adiabatic inversion pulse followed by a TI of 1.2 s was used for T_1 preparation of each slice image. Imaging parameters were a *TE* of 8 ms, *TR* for each segment of 40 ms, a matrix size of 128 × 128, FOV of 20 × 20 cm^2, and a slice thickness of 5 mm. Magnitude correction was performed using navigator echoes.

An advantage of the center-out sampling scheme is the capability of using a short effective echo time, resulting in a high SNR. Especially in the magnetization prepared technique, it is important to acquire the signal with a short *TE*. *TE* of the T_1-weighted images with the center-out scheme was 8 ms, whereas that with the bottom-top scheme was 20.6 ms, resulting in a higher SNR in T_1-weighted images with the center-out scheme. In functional imaging studies, generally *TE* needs to be equal to T_2* of tissue to optimize task-induced signal changes. Thus, the center-out scheme does not provide higher SNR over the bottom-top scheme for fMRI applications. However, the center-out approach reduces flow artifacts. This suppression will increase with increasing number of segments.

EPI images are sensitive to chemical shift artifacts (2, 3, 13). In the readout direction, because each *k*-space line is acquired in a very short time period (less than 1 ms), there is little chemical shift artifact. However, in the phase-encoding direction, each phase-encoding step experiences dephasing cumulatively caused by the chemical shift. This will cause geometric distortions by $\Delta B(x)/G_{pe}$, where $\Delta B(x)$ is the magnetic field inhomogeneity (chemical shift) at the position x and G_{pe} is the blipped gradient strength normalized to the acquisition time. Segmented EPI techniques will have less chemical shift artifacts. In the bottom-top sampling scheme with N_{seg}, the blipped gradient strength increases to $N_{seg} \times G_{pe}$ and thus spatial distortion will be $\Delta B(x)/(N_{seg} \times G_{pe})$. In the center-out segmentation scheme, half of the *k*-space lines is acquired from the center to the top with $G_{pe} \times N_{seg}/2$ gradient strength, resulting in $2 \times \Delta B(x)/(N_{seg} \times G_{pe})$ distortion; and the other half is acquired from the center to the bottom with $-G_{pe} \times N_{seg}/2$, resulting in $-2 \times \Delta B(x)/(N_{seg} \times G_{pe})$ distortion. This finding leads to a more complicated artifact and blurring compared to the segmentation with linear sampling. However, this geometric distortion caused by local susceptibility can be corrected using the acquisition of two images with positive and negative blipped gradients (30). In the center-out segmentation scheme, half of the *k*-space is acquired with the positive blipped gradients and the other half with the negative gradients. Without any additional data collection, geometric distortions caused by local susceptibility can be corrected.

Off-resonance ghosting is a problem in the *ky* direction (2, 3, 13). A large chemical shift from fat cannot be corrected by the aforementioned method (30). In functional imaging studies with a *TE* of 25 ms, fat can be significantly suppressed because of its short T_2* (Fig. 6A). However, in the T_1-weighted images, fat can be problematic because a short *TE* is used. Fat-selective saturation pulses can be inserted between inversion and excitation pulses. This will reduce fat chemical shift artifacts. In the segmented sequences, phase and magnitude discontinuities between segments can exist because of inhomogeneities and T_2* effects, resulting in ghost artifacts. Echo time shifting can reduce phase disconti-

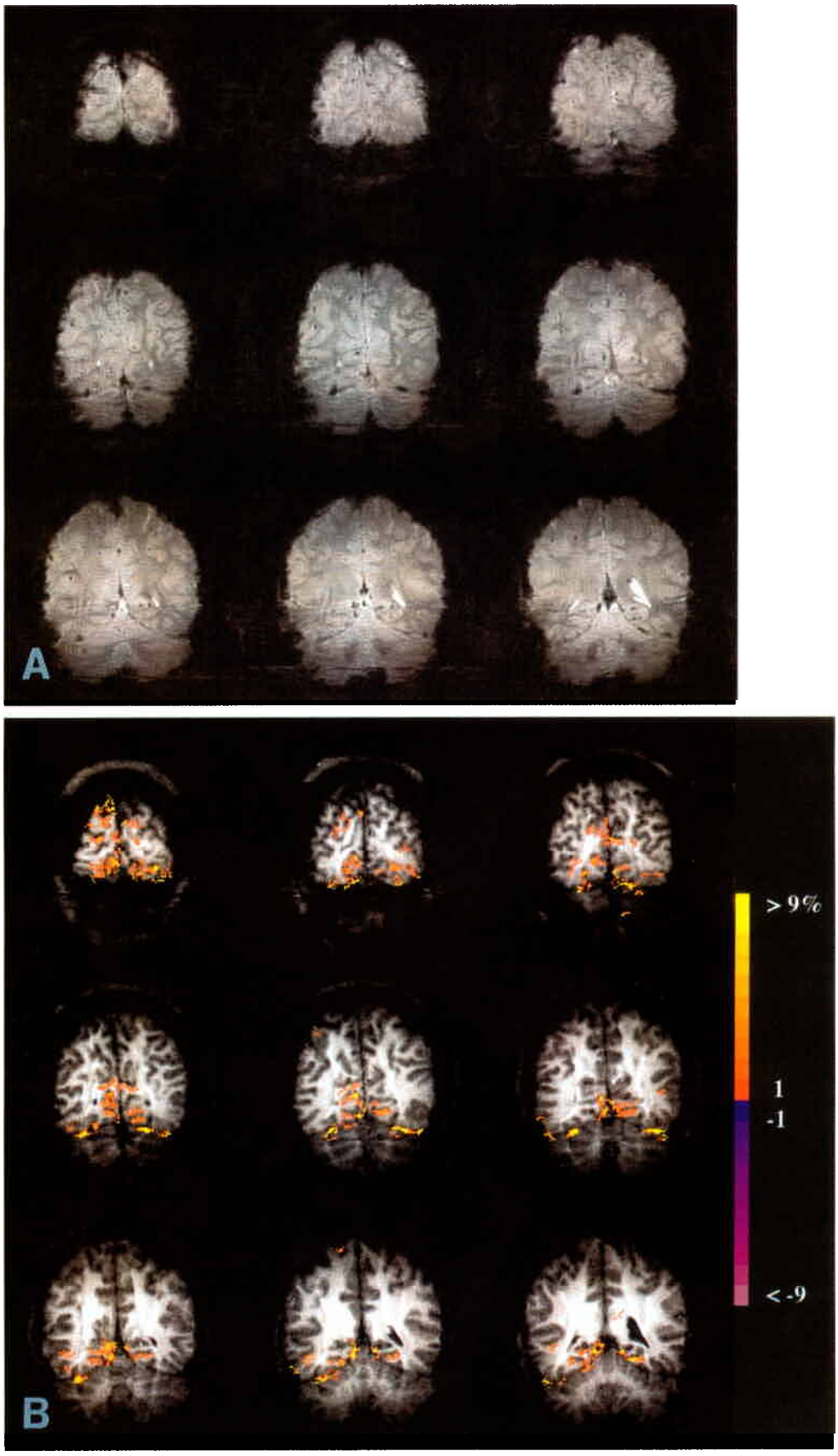

FIG. 6. High-resolution anatomic and functional imaging studies during visual stimulation. (A) Multislice T_1-weighted images with a *TE* of 25 ms and *TR* for each segment of 60 ms. In-plane resolution is 1.56 × 1.56 mm^2 with a slice thickness of 5 mm. For each slice, 75 images were acquired with two stimulation and three control periods; in each period, 15 images were acquired. (B) Functional maps (correlation coefficient > 0.25) overlaid on the T_1-weighted EPI images. Color bar indicates percent signal changes.

nuities (15). In our case where a single *k*-space line was acquired within 1 ms, echo time shifting did not improve image quality significantly.

Because EPI images employ gradient echoes, they will have different T_2^* weighting in each phase-encoding step, causing filtering effects. For example, in the conventional bottom-top *k*-space sampling, the bottom *k*-space line acquired first will have the highest signal intensity and the top *k*-space line acquired last has the least signal intensity. On the other hand, the center-out sampling method has symmetric filtering effects around the center *k*-space line; the center *k*-space line has the short gradient echo time and outer *k*-space lines have longer echo times.

In summary, the interleaved EPI technique with navigator has been developed with center-out phase encoding and variable flip angle schemes. This technique provides high spatial and temporal resolution. It is suitable to obtain high quality anatomic and functional images even at high magnetic field. If both types of images can be acquired using the same imaging pulse sequence with the same gradient strength, functional maps can be overlaid on anatomic images without concerning image misregistration.

ACKNOWLEDGMENTS

The authors thank Dr. Xiao-Hong Zhu for collection of some data, John Strupp for his data processing software (STIMULATE), and Dr. Peter Andersen for hardware support.

REFERENCES

1. P. Mansfield, Multi-planar image formation using NMR spin echoes. *J. Phys. C: Solid State Phys.* **10,** L55 (1977).
2. M. K. Stehling, R. Turner, P. Mansfield, Echo-planar imaging: magnetic resonance imaging in a fraction of a second. *Science* **254,** 43–50 (1991).
3. F. Farzaneh, S. J. Riederer, N. J. Pelc, Analysis of T_2 limitations and off-resonance effects on spatial resolution and artifacts in echo-planar imaging. *Magn. Reson. Med.* **14,** 123–139 (1990).
4. S. Ogawa, D. W. Tank, R. S. Menon, J. M. Ellermann, S.-G. Kim, H. Merkle, K. Ugurbil, Intrinsic signal changes accompanying sensory stimulation: functional brain mapping using MRI. *Proc. Natl. Acad. Sci. (USA),* **89,** 5951–5955 (1992).
5. S.-G. Kim, J. Ashe, A. Georgopoulos, H. Merkle, J. M. Ellermann, R. S. Menon, S. Ogawa, K. Ugurbil, Functional imaging of human motor cortex at high magnetic field. *J. Neurophysiol.* **69,** 297–302 (1993).
6. S.-G. Kim, J. Ashe, K. Hendrich, J. M. Ellermann, H. Merkle, K. Ugurbil, A. Georgopoulos, Functional magnetic resonance imaging of motor cortex: hemispheric asymmetry and handedness. *Science* **261,** 615–617 (1993).
7. S.-G. Kim, K. Ugurbil, P. L. Strick, Activation of a cerebellar output nucleus during cognitive processing. *Science* **265,** 949–951 (1994).
8. K. K. Kwong, J. W. Belliveau, D. A. Chesler, I. E. Goldberg, R. M. Weisskoff, B. P. Poncelet, D. N. Kennedy, B. E. Hoppel, M. S. Cohen, R. Turner, H.-M. Cheng, T. J. Brady, B. R. Rosen, Dynamic magnetic resonance imaging of human brain activity during primary sensory stimulation. *Proc. Natl. Acad. Sci. (USA)* **89,** 5675–5679 (1992).
9. P. A. Bandettini, E. C. Wong, R. S. Hinks, R. S. Tikofsky, J. S. Hyde, Time course EPI of human brain function during task activation. *Magn. Reson. Med.* **25,** 390–397 (1992).
10. R. Turner, P. Jezzard, H. Wen, K. K. Kwong, D. Le Bihan, T. Zeffiro, R. Balaban, Functional mapping of the human visual cortex at 4 and 1.5 Tesla using deoxygenation contrast EPI. *Magn. Reson. Med.* **29,** 277–279 (1993).
11. A. M. Blamire, S. Ogawa, K. Ugurbil, D. Rothman, G. McCarthy, J. Ellermann, F. Hyder, Z. Rattner, R. G. Shulman, Dynamic mapping of the human visual cortex by high-speed magnetic resonance imaging. *Proc. Natl. Acad. Sci. (USA)* **89,** 11069–11073 (1992).
12. J. Frahm, K. D. Merboldt, W. Hanicke, Functional MRI of human brain activation at high spatial resolution. *Magn. Reson. Med.* **29,** 139–144 (1993).
13. G. C. McKinnon, Ultrafast interleaved gradient-echo-planar imaging on a standard scanner. *Magn. Reson. Med.* **30,** 609–616 (1993).
14. K. Butts, S. J. Riederer, R. L. Ehman, R. T. Thompson, C. R. Jack, Interleaved echo planar imaging on a standard MRI system. *Magn. Reson. Med.* **31,** 67–72 (1994).
15. Z. H. Cho, C. B. Ahn, J. H. Kim, Y. E. Lee, C. W. Mun, Phase error corrected interlaced echo planar imaging, *in* "Proc., SMRM, 6th Annual Meeting, 1987," p. 912.
16. S. G. Tan, A. W. Song, E. C. Wong, J. S. Hyde, S.-J. Li, High resolution fMRI with interleaved EPI, *in* "Proc., SMR, 3rd Meeting, 1995," p. 796.
17. J. Frahm, A. Haase, D. Matthaei, K.-D. Merboldt, W. Hanicke, Rapid NMR imaging using stimulated echoes. *J. Magn. Reson.* **65,** 130–135 (1985).
18. D. G. Norris, Excitation angle optimization for snapshot FLASH and a signal comparison with EPI. *J. Magn. Reson.* **91,** 190–193 (1991).
19. X. Hu, S.-G. Kim, Reduction of signal fluctuation in functional MRI using navigator echoes. *Magn. Reson. Med.* **31,** 495–503 (1993).
20. R. L. Ehman, J. P. Felmlee, Adaptive technique for high-definition MR imaging of moving structures. *Radiology* **173,** 255–263 (1989).
21. J. L. Duerk, O. P. Simonetti, Theoretical aspects of motion sensitivity and compensation in echo-planar imaging. *J. Magn. Reson. Imaging* **1,** 643–650 (1991).
22. K. Butts, S. J. Riederer, Analysis of flow effects in echo-planar imaging. *J. Magn. Reson. Imaging* **2,** 285–293 (1992).
23. O. P. Simonetti, P. Wielopolski, J. L. Duerk, Experimental evaluation of flow effects in echo planar imaging, *in* "Proc., SMR, 2nd Meeting, 1994," p. 460.
24. G. T. LuK Pat, D. G. Nishimura, Reducing flow artifacts in echo-planar imaging, *in* "Proc., SMR, 2nd Meeting, 1994," p. 473.
25. H. Bruder, H. Fischer, H.-E. Reinfelder, F. Schmitt, Image reconstruction for echo planar imaging with nonequivalent k-space sampling. *Magn. Reson. Med.* **23,** 311–323 (1992).
26. S.-G. Kim, X. Hu, K. Ugurbil, Accurate T_1 determination from inversion recovery images: application to human brain at 4 Tesla. *Magn. Reson. Med.* **31,** 445–449 (1994).
27. P. A. Bandettini, A. Jesmanowicz, E. C. Wong, J. S. Hyde, Processing strategies for time-course data sets in functional MRI of the human brain. *Magn. Reson. Med.* **30,** 161–173 (1993).
28. R. M. Weisskoff, J. Baker, J. Belliveau, T. L. Davis, K. K. Kwong, M. S. Cohen, B. R. Rosen, Power spectrum analysis of functionally weighted MR data: what's in the noise? *in* "Proc., SMRM, 12th Meeting, 1993," p. 7.
29. X. Hu, T. H. Le, T. Parrish, P. Erhard, Retrospective estimation and compensation of physiological fluctuation in functional MRI. *Magn. Reson. Med.* **34,** 210–221 (1995).
30. R. Bowtell, D. J. O. McIntyre, M-J. Commandre, P. M. Glover, P. Mansfield, Correction of geometric distortion in echo planar images, *in* "Proc., SMR, 2nd Meeting, 1994," p. 411.